

# Naval Surface Warfare Center, Carderock Division

Bethesda, MD 20084-5000

---

CRDKNSWC/HD-1362-03 June 1996

Hydromechanics Directorate  
Research and Development Report

## Application of an Upwind High Resolution Finite-Differencing Scheme and Multigrid Method in Steady-State Incompressible Flow Simulations

by  
Cheng-I Yang,  
NSWCCD, David Taylor Model Basin

Yanhu Guo, Chaoqun Liu  
University of Colorado at Denver

C-H Liu  
NASA/Langley Research Center

19961023 265

CRDKNSWC/HD-1362-03 Application of an Upwind High Resolution Finite-Differencing Scheme  
and Multigrid Method in Steady-State Incompressible Flow Simulations



---

Approved for public release; distribution is unlimited.

## MAJOR CARDEROCK DIVISION TECHNICAL COMPONENTS

- CODE 011 Director of Technology
- 10 Machinery Systems/Programs and Logistics Directorate
  - 20 Ship Systems and Programs Directorate
  - 50 Hydromechanics Directorate
  - 60 Survivability, Structures and Materials Directorate
  - 70 Signatures Directorate
  - 80 Machinery Research and Development Directorate
  - 90 Machinery In-Service Engineering Directorate

### CARDEROCK DIVISION, NSW, ISSUES THREE TYPES OF REPORTS:

1. **CARDEROCKDIV reports, a formal series**, contain information of permanent technical value. They carry a consecutive numerical identification regardless of their classification or the originating directorate.
2. **Directorate reports, a semiformal series**, contain information of a preliminary, temporary, or proprietary nature or of limited interest or significance. They carry an alphanumerical identification issued by the originating directorate.
3. **Technical memoranda, an informal series**, contain technical documentation of limited use and interest. They are primarily working papers intended for internal use. They carry an identifying number which indicates their type and the numerical code of the originating directorate. Any distribution outside CARDEROCKDIV must be approved by the head of the originating directorate on a case-by-case basis.

# REPORT DOCUMENTATION PAGE

*Form Approved*  
OMB No. 0704-0188

*Public Reporting burden for this collection of information is estimated to average 1 hour per response, including the time for reviewing instructions, searching existing data sources, gathering and maintaining the data needed, and completing and reviewing the collection of information. Send comments regarding this burden estimate or any other aspect of this collection of information, including suggestions for reducing this burden, to Washington Headquarters Services, Directorate for Information Operations and Reports 1215 Jefferson Davis Highway, Suite 1204, Arlington, VA 22202-4302, and to Office of Management and Budget, Paperwork Reduction Project (0704-0188), Washington, DC 20503*

1. AGENCY USE ONLY (Leave Blank)		2. REPORT DATE June 1996		3. REPORT TYPE AND DATE COVERED Final	
4. TITLE AND SUBTITLE Application of an Upwind High Resolution Finite-Differencing Scheme and Multigrid Method in Steady-State Incompressible Flow Simulations				5. FUNDING NUMBERS XXXXX	
6. AUTHOR(S) Yang, Cheng-I, NSWCCD, David Taylor Model Basin; Guo, Yanhu and Liu, Chaoqun, University of Colorado at Denver, and Liu, C-H, NASA Langley Research Center					
7. PERFORMING ORGANIZATION NAME(S) AND ADDRESS(ES) Naval Surface Warfare Center, Carderock Division Code 544 Bethesda, Maryland 20084-5000				8. PERFORMING ORGANIZATION REPORT NUMBER CRDKNSWC/HD-1362-03	
9. SPONSORING / MONITORING AGENCY NAME(S) AND ADDRESS(ES) Office of Naval Research ONR334 800 N. Quincy St. Arlington, Virginia 22217-5660				10. SPONSORING / MONITORING AGENCY REPORT NUMBER	
11. SUPPLEMENTARY NOTES					
12a. DISTRIBUTION / AVAILABILITY STATEMENT Approved for public release; distribution is unlimited.				12b. DISTRIBUTION CODE	
13. ABSTRACT (Maximum 200 words)  The analysis and design of a submarine propulsor requires the ability to predict the characteristics of both laminar and turbulent flows to a higher degree of accuracy. This report presents results of certain benchmark computations based on an upwind, high-resolution, finite-differencing Navier-Stokes solver. The purpose of the computations is to evaluate the ability, the accuracy and the performance of the solver in the simulation of detailed features of viscous flows. Features of interest include flow separation and reattachment, surface pressure and skin friction distributions. Those features are particularly relevant to the propulsor analysis. Test cases with a wide range of Reynolds numbers are selected; therefore, the effects of the convective and the diffusive terms of the solver can be evaluated separately. Test cases include flows over bluff bodies, such as circular cylinders and spheres, at various low Reynolds numbers, flows over a flat plate with and without turbulence effects, and turbulent flows over axisymmetric bodies with and without propulsor effects. Finally, to enhance the iterative solution procedure, a full approximation scheme V-cycle multigrid method is implemented. Preliminary results indicate that the method significantly reduces the computational effort.					
14. SUBJECT TERMS Navier-Stokes Equations, High-Resolution Upwind Finite-Differencing Scheme, Multigrid Method, Flow Over Bluff Bodies				15. NUMBER OF PAGES 35	
				16. PRICE CODE	
17. SECURITY CLASSIFICATION OF REPORT UNCLASSIFIED		18. SECURITY CLASSIFICATION OF THIS PAGE UNCLASSIFIED		19. SECURITY CLASSIFICATION OF ABSTRACT UNCLASSIFIED	
				20. LIMITATION OF ABSTRACT Same as report	

## CONTENTS

	Page
<b>Abstract</b> .....	1
<b>Administrative Information</b> .....	1
<b>Introduction</b> .....	1
<b>The Governing Equations</b> .....	3
<b>Numerical Discretization</b> .....	4
Inviscid Fluxes .....	5
Viscous Fluxes .....	7
<b>Solution Algorithm</b> .....	7
<b>Multigrid Method</b> .....	8
<b>Solution Procedure</b> .....	8
<b>Results</b> .....	9
Turbulent Flow Along a Flat Plate .....	9
Laminar Flow Along a Flat Plate .....	11
Flow Past Circular Cylinders at Low Speeds .....	13
Flow Past Spheres at Low Speed .....	19
Turbulent Flow Past Axisymmetric Bodies .....	21
<b>Conclusions and Recommendations</b> .....	27
<b>References</b> .....	27

## FIGURES

1. Skin friction coefficient and velocity profile for turbulent flow along a flat plate .....	10
2. Velocity profile in $y^+.u^+$ .....	11
3. Convergence histories for computing turbulent flow along a flat plate .....	11
4. Skin friction coefficient and velocity profiles for laminar flow along a flat plate .....	12
5. Convergence histories for computing laminar flow along a flat plate .....	13
6. Geometrical parameters of the closed wake .....	14

## FIGURES (Cont'd)

	Page
7. Standing vortices downstream of a circular cylinder .....	15
8. Separation angles at different Reynolds numbers for flow past a circular cylinder .....	16
9. Wake lengths at different Reynolds numbers for flow past a circular cylinder .....	16
10. Locations of vortex centers of wakes at different Reynolds numbers .....	17
11. Similarity of the closed-wake shapes .....	17
12. Velocity similarity on the rear flow axes of the closed wakes .....	17
13. Velocity distributions on the flow axis behind the circular cylinder .....	18
14. Surface pressure distribution for flow past a circular cylinder at $Re=40$ .....	18
15. Convergence histories for computing flow past a circular cylinder at $Re=40$ .....	18
16. Standing vortices downstream of a sphere .....	19
17. Wake lengths at different Reynolds numbers for flow past a sphere .....	20
18. Surface pressure distribution for flow past a sphere at $Re = 100$ .....	20
19. Convergence histories for computing flow past a sphere at $Re=100$ .....	20
20. Surface pressure distribution for DTMB-body1 .....	21
21. Velocity profiles at stern region of DTMB-body1 .....	22
22. Comparisons of wall law at mid-body section of DTMB-body1 .....	23
23. Skin friction coefficient along the surface of DTMB-body1 .....	23
24. Turbulent shear stresses near the stern region of DTMB body1 .....	24
25. Velocity profiles upstream of an operating propeller at different advance ratios .....	25
26. Velocity profiles at stern region of DTMB-body2 .....	26

## ABSTRACT

*The analysis and design of a submarine propulsor requires the ability to predict the characteristics of both laminar and turbulent flows to a high degree of accuracy. This report presents results of certain benchmark computations based on an upwind, high-resolution, finite-differencing Navier-Stokes solver. The purpose of the computations is to evaluate the ability, the accuracy and the performance of the solver in the simulation of detailed features of viscous flows. Features of interest include flow separation and reattachment, surface pressure and skin friction distributions. Those features are particularly relevant to the propulsor analysis. Test cases with a wide range of Reynolds numbers are selected; therefore, the effects of the convective and the diffusive terms of the solver can be evaluated separately. Test cases include flows over bluff bodies, such as circular cylinders and spheres, at various low Reynolds numbers, flows over a flat plate with and without turbulence effects, and turbulent flows over axisymmetric bodies with and without propulsor effects. Finally, to enhance the iterative solution procedure, a full approximation scheme V-cycle multigrid method is implemented. Preliminary results indicate that the method significantly reduces the computational effort.*

## ADMINISTRATIVE INFORMATION

This investigation was authorized by the Office of Naval Research under 6.2 Viscous Flow Program, in accordance with Program Element 62323N, Task Area R2332MS3, and Work Request Number N001495WX20047/AJ. This work was performed at the Naval Surface Warfare Center, Carderock Division (NSWCCD), David Taylor Model Basin (DTMB) under Work Unit 5060-567.

## INTRODUCTION

Hydrodynamically speaking, propulsor components are lifting bodies that provide thrust for propulsion. To improve the propulsive performance, it is desirable to have a lifting body with an optimum lift to drag ratio. Successful analysis and design requires the ability to predict the hydrodynamic forces on the lifting body, such as lift and drag, to a high degree of accuracy. Recently, large research efforts on computational fluid dynamics (CFD) have been directed to achieve such goals. The most practical approach is to derive some numerical methods for the Reynolds-averaged Navier-Stokes equations (RANS). The more popular methods, depending on the manner the convective terms are formulated, include the central differencing and the upwind differencing schemes. Both upwind (DTNS Code<sup>1</sup>) and central (IFLOW Code<sup>2</sup>) differencing formulations have been used for hydrodynamics simulations at the David Taylor Model Basin (DTMB). As part of DTMB propulsor research efforts, a variation of the upwind schemes has been employed to simulate the flow through the blade rows of a turbomachinery<sup>3, 4</sup>.

For high Reynolds number flows, the Navier-Stokes equations become convectively dominated and are hyperbolic in nature. Under such circumstances, the upwind differencing approach becomes attractive and has certain advantages. For a one-dimensional case, it can be shown that the information at any point propagates in the direction according to the sign of the local eigenvalues of the flux Jacobian. Consequently, a numerical procedure with the upwind differencing technique based on the direction of local wave propagation is physically more adaptive to the characteristics of the equations. Besides, in the upwind scheme, the dispersive and dissipative errors are more closely balanced than in other schemes of equal or even higher order that use the same set of nodal points, regardless of the direction of the convection<sup>5</sup>. The flux-differencing splitting approach suggested by Roe<sup>6</sup> is a popular upwind scheme for solving the incompressible Navier-Stokes equations, since it does not require the inviscid flux to be a homogenous function of order one. Based on Roe's approach<sup>6</sup> the flux-difference is split according to an approximate solution of the Riemann problem. The solution provides the information about the direction of the wave propagation, which, in turn, is incorporated into the discretized system to form an upwind scheme. The accuracy of the solution can be promoted to a higher order by reconstructing the primitive variables or the fluxes midway between two nodes with an extrapolation technique. In conjunction with the reconstruction process, the slope limiter or the flux limiter can be implemented to obtain total variation diminishing (TVD) property<sup>7</sup>. Viscous terms can be discretized with a second order central differencing scheme. A numerical formulation, based on the principles described above, allows the discontinuity of the solution to be resolved over only two adjacent nodes without causing the non-physical oscillations. Therefore, this approach is sometimes called high resolution.

This report presents the results of a numerical study designed to evaluate the ability and accuracy of an upwind scheme in predicting certain flow features that are relevant to propulsor analysis. Some of the features of interest are flow separation and reattachment, surface pressure and skin friction distribution. Test cases for present numerical study are selected so that (1) a wide range of Reynolds numbers are covered, (2) the boundaries are smooth and the distortions of the grid systems are minimized, (3) the flow features are relevant to the propulsor analysis and (4) the test data are well analyzed. Test cases include flows over bluff bodies, such as circular cylinders and spheres, at various low Reynolds numbers, flows over a flat plate with and without turbulence effects, and turbulent flows over axisymmetric bodies with and without propulsor effects. To enhance the iterative solution procedure, a full approximation scheme (FAS) V-cycle multigrid method is implemented. A fast convergence rate is achieved as a result.

## THE GOVERNING EQUATIONS

The three-dimensional incompressible RANS equations based on primitive variables are formulated in a boundary-fitted curvilinear coordinate system. Using Chorin's artificial compressibility formulation,<sup>8</sup> the incompressible Navier-Stokes equation is written in conservation form for three-dimensional flow in Cartesian system as

$$Q_t + (E^* - E_v^*)_x + (F^* - F_v^*)_y + (G^* - G_v^*)_z = 0 \quad (1)$$

In Eq. 1, the dependent variable vector  $Q$  is defined as  $Q = (p, u, v, w)^T$ , and the inviscid flux vectors  $E^*$ ,  $F^*$ , and  $G^*$ , the viscous shear flux vectors  $E_v^*$ ,  $F_v^*$ , and  $G_v^*$  are given by

$$\begin{aligned} E^* &= (\beta u, u^2 + p, uv, uw)^T \\ F^* &= (\beta v, uv, v^2 + p, vw)^T \\ G^* &= (\beta w, uw, vw, w^2 + p)^T \\ E_v^* &= Re^{-1}(0, 2u_x, u_y + v_x, u_z + w_x)^T \\ F_v^* &= Re^{-1}(0, u_y + v_x, 2v_y, v_z + w_y)^T \\ G_v^* &= Re^{-1}(0, u_z + w_x, v_z + w_y, 2w_z)^T. \end{aligned}$$

The coordinates  $x, y, z$  are scaled with an appropriate characteristic length scale  $L$ . The Cartesian velocity components  $u, v, w$  are nondimensionalized with respect to the free stream velocity,  $V_\infty$ . The normalized pressure is defined as  $p = (p - p_\infty)/\rho V_\infty^2$ . The kinematic viscosity,  $\nu$ , is assumed to be constant, and the Reynolds number is defined as  $Re = V_\infty L/\nu$ . The artificial compressibility parameter,  $\beta$ , monitors the error associated with the addition of the unsteady pressure term  $\partial p/\partial t$  in the continuity equation. The unsteady pressure term is needed for coupling the mass and momentum equations to make the system hyperbolic.

Equation 1 can be transferred to a curvilinear, body-fitted coordinate system  $(\zeta, \xi, \eta)$  through a coordinate transformation of the form

$$\zeta = \zeta(x, y, z), \quad \xi = \xi(x, y, z), \quad \text{and} \quad \eta = \eta(x, y, z).$$

Thus, Eq. 1 becomes,

$$(Q/J)_t + (E - E_v)_\zeta + (F - F_v)_\xi + (G - G_v)_\eta = 0 \quad (2)$$

with

$$(E, F, G)^T = \{ [T] (E^*/J, F^*/J, G^*/J)^T \}$$

and

$$(E_v, F_v, G_v)^T = [T] (E_v^*/J, F_v^*/J, G_v^*/J)^T,$$

where

$$[T] = \begin{bmatrix} \zeta_x & \zeta_y & \zeta_z \\ \xi_x & \xi_y & \xi_z \\ \eta_x & \eta_y & \eta_z \end{bmatrix}$$

and the Jacobian of the coordinate transformation is given by

$$J^{-1} = \det \begin{bmatrix} x_\zeta & y_\zeta & z_\zeta \\ x_\xi & y_\xi & z_\xi \\ x_\eta & y_\eta & z_\eta \end{bmatrix}$$

The Jacobian is the ratio of volume elements in the two coordinate systems. For a proper transformation, neither  $J$  nor its reciprocal is zero. At present, the transformation is chosen so that the grid spacing in the computational domain is uniform and of one unit in length in all three spatial directions. The Cartesian derivatives of the shear fluxes are obtained by expanding them using chain rule expansions in the  $\zeta$ ,  $\xi$ , and  $\eta$  directions.

## NUMERICAL DISCRETIZATION

Let  $i, j, k$  denote the integer indices of a grid point in the curvilinear system  $\zeta, \xi, \eta$  whose Cartesian coordinates are  $x, y, z$ . Each grid point serves also as the centroid of a control volume whose six bounding surfaces are formed by bisecting the distances between the centroid and its six adjacent grid points. The Cartesian flow variables such as  $u, v, w$  and  $p$  are placed at each grid point. The indices of the grid point are used as subscripts for the variables to indicate the association. To avoid introducing any free stream error, the metric terms such as  $\zeta_x, \xi_x$  and  $\eta_x$  etc., are computed from  $x, y, z$  data by using a second-order central-differencing approximation of  $x_\zeta, x_\xi$  and  $x_\eta$  etc., as described by Pulliam and Steger<sup>9</sup>.

## INVISCID FLUXES

At present, discretization of the inviscid fluxes of Eq. 2 is achieved by applying the Riemann solver to each direction of the coordinate system as suggested by Yee, Warming and Harten<sup>10</sup>. Consider a one-dimensional hyperbolic system of conservative laws

$$\left(\frac{Q}{J}\right)_t + H_\theta(Q) = 0, \quad D(Q) = \frac{\partial H}{\partial Q}, \quad (3)$$

where  $\theta = \zeta, \xi$  or  $\eta$ , and  $D(Q)$  is the Jacobian Matrix. Both  $Q$  and  $H(Q)$  are column vectors with four components and  $D(Q)$  is a four by four matrix.

Let the right eigenvectors be the column elements of matrix  $R$  and eigenvalues  $\lambda_1, \lambda_2, \lambda_3$  and  $\lambda_4$  be the diagonal elements of matrix  $\Lambda$ , then the relationship between  $D, R$  and  $\Lambda$  is given by a similarity transformation  $D = R\Lambda R^{-1}$ . The row elements

of the matrix  $R^{-1}$  give an orthonormal set of the left eigenvectors. In the discretized system, the state  $Q_l$  at grid point  $l$  is considered as an averaged value in an interval, that is

$$Q_l = \Delta\theta^{-1} \int_{(l-\frac{1}{2})\Delta\theta}^{(l+\frac{1}{2})\Delta\theta} Q d\theta. \quad (4)$$

Roe's flux difference splitting is constructed by forming a mean value Jacobian  $\hat{D}(Q_{l+1}, Q_l)$  such that

$$H(Q_{l+1}) - H(Q_l) = \hat{D}(Q_{l+1}, Q_l) (Q_{l+1} - Q_l),$$

and

$$\hat{D}(Q_{l+1}, Q_l) = D(Q_{l+1}, Q_l) \quad \text{as} \quad Q_{l+1} \rightarrow Q_l.$$

to evaluate the mean value (the local frozen value) Jacobian at the interface  $l \pm \frac{1}{2}$ , the simple average value of the state  $Q$  at two adjacent grid points are used, that is

$$\hat{D}_{l \pm \frac{1}{2}} = D_{l \pm \frac{1}{2}}(Q_{l \pm \frac{1}{2}}) \quad (5)$$

where

$$Q_{l \pm \frac{1}{2}} = \frac{1}{2}(Q_l \pm Q_{l \pm 1})$$

By the similarity transformation,  $D_{l \pm \frac{1}{2}}$  can be written as

$$\begin{aligned} D_{l \pm \frac{1}{2}} &= (R\Lambda R^{-1})_{l \pm \frac{1}{2}} \\ &= (R\Lambda^+ R^{-1})_{l \pm \frac{1}{2}} - (R\Lambda^- R^{-1})_{l \pm \frac{1}{2}} \\ &= D_{l \pm \frac{1}{2}}^+ - D_{l \pm \frac{1}{2}}^- , \end{aligned}$$

where  $\Lambda^+$  and  $\Lambda^-$  are the absolute values of the positive (speed of the right travelling wave) and the negative (speed of the left travelling wave) eigenvalues, respectively. With the mean value Jacobian locally defined, Eq. 3 can be decoupled into a system of four scalar equations with the eigenvalues representing the wave speeds of the Riemann problem. Let's define the local characteristic variables  $W$  as the projection of  $Q$  into the left eigenvectors  $R^{-1}$ ; therefore,  $W = R^{-1}Q$ . For any given two states  $Q_l$  and  $Q_{l+1}$ , the flux at the interface  $H_{l \pm \frac{1}{2}}$  can be expressed, in term of flux difference, as either

$$H_{l \pm \frac{1}{2}} = H_l + R\Lambda^- \Delta_{l \pm \frac{1}{2}} W \quad (6)$$

or

$$H_{l \pm \frac{1}{2}} = H_{l+1} - R\Lambda^+ \Delta_{l \pm \frac{1}{2}} W , \quad (7)$$

where  $\Delta_{l+\frac{1}{2}}W = (W_{l+1} - W_l)/2$  .

Assuming that  $R, R^{-1}$  and  $\Lambda$  are constant, with Eqs 6 and 7, Eq. 3 can be written as a system of four scalar hyperbolic conservative equations for the characteristic variables  $W$  , that is,

$$\left(\frac{W_m}{J}\right)_t - (\lambda_m^-)_{l+\frac{1}{2}}\Delta_{l+\frac{1}{2}}W_m + (\lambda_m^+)_{l-\frac{1}{2}}\Delta_{l-\frac{1}{2}}W_m = 0 \quad \text{for } m = 1, 2, 3, 4. \quad (8)$$

An implicit delta form of Eq. 8 is

$$\begin{aligned} & \left[ \frac{1}{\tau J} - (\lambda_m^-)_{l+\frac{1}{2}}\Delta_{l+\frac{1}{2}} + (\lambda_m^+)_{l-\frac{1}{2}}\Delta_{l-\frac{1}{2}} \right] \Delta W_m^n \\ & = (\lambda_m^-)_{l+\frac{1}{2}}\Delta_{l+\frac{1}{2}}W_m^n - (\lambda_m^+)_{l-\frac{1}{2}}\Delta_{l-\frac{1}{2}}W_m^n , \end{aligned} \quad (9)$$

where  $\tau$  is the time step size,  $n$  is the time step number, and  $\Delta W_m^n = W_m^{n+1} - W_m^n$ .

When  $W_m^n$  is sufficiently differentiable, the local jump in  $W_m^n$  at the interfaces  $l \pm \frac{1}{2}$ , known as

$$\Delta_{l\pm\frac{1}{2}}W_m^n \quad (10)$$

are replaced with

$$\left(\frac{\partial W_m}{\partial \theta}\right)_{l\pm\frac{1}{2}}^n \Delta \theta . \quad (11)$$

Equation 10 is only a first-order one-sided approximation of Eq. 11. To enhance the accuracy, the following relationships from a scalar scheme can be extended to a constant coefficient system by applying them scalarly to each of the  $m$  scalar characteristic components in Eq. 8,

$$\begin{aligned} & \left(\frac{\partial W_m}{\partial \theta}\right)_{l-\frac{1}{2}}^n \Delta \theta = \left(W_{m,l}^n - W_{m,l-1}^n\right) \\ & + \frac{1}{4} \left[ (1 + \omega)(\Phi_{m,l+1}^- - \Phi_{m,l}^+) \Delta_{l+\frac{1}{2}}W_m^n + (1 - \omega)(\Phi_{m,l}^- - \Phi_{m,l-1}^+) \Delta_{l-\frac{1}{2}}W_m^n \right] , \end{aligned} \quad (12)$$

and

$$\begin{aligned} & \left(\frac{\partial W_m}{\partial \theta}\right)_{l+\frac{1}{2}}^n \Delta \theta = \left(W_{m,l+1}^n - W_{m,l}^n\right) \\ & - \frac{1}{4} \left[ (1 + \omega)(\Phi_{m,l}^- - \Phi_{m,l-1}^+) \Delta_{l-\frac{1}{2}}W_m^n + (1 - \omega)(\Phi_{m,l+1}^- - \Phi_{m,l}^+) \Delta_{l+\frac{1}{2}}W_m^n \right] , \end{aligned} \quad (13)$$

for  $m=1,2,3,4$ , with

$$\Phi_{m,l}^\pm = \Phi(r_{m,l}^\pm) , \quad (14)$$

and

$$r_{m,l}^{\pm} = \begin{cases} (\Delta_{l-\frac{1}{2}} W_m^n / \Delta_{l+\frac{1}{2}} W_m^n)^{\pm} & \text{for } \Delta_{l\pm\frac{1}{2}} W_m^n \neq 0 \\ 0 & \text{for } \Delta_{l\pm\frac{1}{2}} W_m^n = 0 \end{cases} \quad (15)$$

The order of the accuracy in the spatial derivatives presented above is determined by the values of  $\omega$ . For  $\omega = -1$ , the scheme is fully upwind second-order accurate. For  $\omega = \frac{1}{3}$ , the scheme is upwind biased third-order accurate. Function  $\Phi$  is called the limiter; it is used to control unwanted oscillations in numerical schemes. Various designs of the limiter were found and successfully tested.<sup>3, 11</sup>

Substitute Eqs. 12 and 13 into Eq. 9, and multiply Eq. 9 by the set of right eigenvectors  $R$  from the left. A conservative high-resolution scheme for the nonlinear system is derived:

$$\left[ \left( \frac{I}{\Delta t J} \right) - (D_{l+\frac{1}{2}}^- \Delta_{l+\frac{1}{2}} - D_{l-\frac{1}{2}}^+ \Delta_{l-\frac{1}{2}})^n \right] \Delta Q^n = \\ (RK^{-1}R^{-1})_{l+\frac{1}{2}}^n \Delta_{l+\frac{1}{2}} Q^n - (RK^{+1}R^{-1})_{l-\frac{1}{2}}^n \Delta_{l-\frac{1}{2}} Q^n, \quad (16)$$

with

$$K_{l\pm\frac{1}{2}}^{\mp} = \pm \left[ \Lambda_{l\pm\frac{1}{2}}^{\mp} - [(1-\omega)\Lambda_{l\pm\frac{1}{2}}^{\mp} + (1+\omega)\Lambda_{l\pm\frac{1}{2}}^{\pm}] (\Phi_{l\pm 1}^{\mp} - \Phi_l^{\pm}) / 4 \right]^n,$$

and

$$\Phi_l^{\pm} = \text{diag}(\Phi_1^{\pm}, \Phi_2^{\pm}, \Phi_3^{\pm}, \Phi_4^{\pm})_l$$

The right hand side of the Eq. 16 is evaluated at time level  $n$ ; it is the spatial derivative of Eq. 2 and is designated as residual. Equation 16 represents the relationship between the residual at  $n^{\text{th}}$  time step and the correction of the solutions at  $n+1^{\text{th}}$  time step. The correction and the residual approach to zero as the solutions approach to their steady state values.

## VISCOUS FLUXES

The viscous fluxes in Eq. 2 are evaluated by a second-order central differencing scheme. The computation of the fluxes require all nine metric coefficients at each of the six bounding surfaces of each computational cell.

## SOLUTION ALGORITHM

Equation 16 can be extended to three-dimensional applications with the operator split method. The differencing schemes described previously are applied to each coordinate direction  $\zeta$ ,  $\xi$ , and  $\eta$  independently; a summation over all directions gives the discretized approximation of a multi-dimensional flow problem. Upon forming the Jacobian matrices  $A$ ,  $B$ , and  $C$  from invicid fluxes  $E$ ,  $F$ , and  $G$  and  $X$ ,  $Y$ , and

$Z$  from the viscous fluxes  $E_v$ ,  $F_v$ , and  $G_v$ , a finite-differencing form of Navier-Stokes equations can then be written as:

$$\left( \frac{I}{\tau J} - (A^- + X)_{i+\frac{1}{2}} \Delta_{i+\frac{1}{2}} + (A^+ + X)_{i-\frac{1}{2}} \Delta_{i-\frac{1}{2}} - (B^- + Y)_{j+\frac{1}{2}} \Delta_{j+\frac{1}{2}} + (B^+ + Y)_{j-\frac{1}{2}} \Delta_{j-\frac{1}{2}} - (C^- + Z)_{k+\frac{1}{2}} \Delta_{k+\frac{1}{2}} + (C^+ + Z)_{k-\frac{1}{2}} \Delta_{k-\frac{1}{2}} \right)^n \Delta Q^n = -RES(Q^n) . \quad (17)$$

Equation 17 is solved by an implicit hybrid algorithm where a symmetric planar Gauss-Seidel relaxation is used in the  $\zeta$  direction and approximation factorization is applied in the  $\xi$  and  $\eta$  directions:

$$\left[ M - (B^- + Y)_{j+\frac{1}{2}} \Delta_{j+\frac{1}{2}} + (B^+ + Y)_{j-\frac{1}{2}} \Delta_{j-\frac{1}{2}} \right] \Delta \tilde{Q} = -RES(Q^n, Q^{n+1}) , \quad (18)$$

$$\left[ M - (C^- + Z)_{k+\frac{1}{2}} \Delta_{k+\frac{1}{2}} + (C^+ + Z)_{k-\frac{1}{2}} \Delta_{k-\frac{1}{2}} \right] \Delta Q = M \Delta \tilde{Q} , \quad (19)$$

$$Q^{n+1} = Q^n + \Delta Q^n , \quad (20)$$

with  $M = I/(\tau J) + (A^- + X)_{i+\frac{1}{2}} + (A^+ + X)_{i-\frac{1}{2}}$ , where  $RES(Q^n, Q^{n+1})$  indicates the nonlinear updating of the residual while sweeping in the  $\zeta$  direction.

## MULTIGRID METHOD

For certain simulations, in order to obtain meaningful results, a large number of finely sized grid points is needed. The adverse effect of such a grid system upon the computation effort is that the rate of convergence deteriorates significantly. The analysis provided by Brandt<sup>12</sup> suggests that the low-frequency components of the errors are efficiently approximated on coarse grids but are slow to convergence on fine grids. In addition, the high-frequency components must be approximated on fine grids. By utilizing interactively several scales of discretization, multigrid techniques resolve such conflicts and avoid stalling.

To accommodate nonlinearities, a full approximate scheme (FAS) is used. The discretized system of equations described previously can be represented as:

$$L(Q) = -R , \quad (21)$$

where  $L$  is the differencing operator,  $Q$  is the unknown to be solved and  $R$  is the residual. The iterative process will reduce the residual to zero as the steady-state solution is approached. The FAS procedures for solving Eq. 21 can be described as follows:

- (1) relax on the fine grid,  $L_h(Q^h) = -R^h$  ,

- (2) solve  $L_{2h}(Q^{2h}) + [\tilde{I}_h^{2h}[L_h(Q^h)] - L_{2h}(I_h^{2h}Q^h)] = -R^{2h}$  on the coarse grid, and  
 (3) replace  $Q^h \leftarrow Q^h + I_{2h}^h(Q^{2h} - I_h^{2h}Q^h)$  on the fine grid.

The notation introduced here includes the difference operators at the fine grid  $L_h$  and the coarse grid  $L_{2h}$ , the restriction operators  $I_h^{2h}$  (for the approximation) and  $\tilde{I}_h^{2h}$  (for the residual), and the interpolation operator  $I_{2h}^h$ .

## RESULTS

In the followings benchmark computations, in order to qualify the comparison between the experimental measurements and computational results, root-mean-square (RMS) differences<sup>2</sup> are calculated. The RMS difference is defined as

$$RMS = \left[ \sum_i^N (v_i^c - v_i^m)^2 / N \right]^{\frac{1}{2}},$$

where  $v^c$  and  $v^m$  are computed and measured values respectively,  $N$  is the total number of data values used in the comparison, and the subscript  $i$  ranges from 1 to  $N$ . Computations were carried out with 64-bit precision on a Silicon Graphics Power Challenge machine.

### TURBULENT FLOW ALONG A FLAT PLATE

The structure of the turbulent boundary layer along a flat plate has been investigated earlier by Ludweig and Tillmann<sup>13</sup>, and Wieghart and Tillmann<sup>14</sup>. It was found that the axial velocity profile in the inner one-fifth of the boundary layer can be represented by the universal logarithmic law (excluding the viscous sublayer). The remaining outer four-fifths can be adequately expressed by the power law. Wieghart and Tillmann's data were collected in a wind tunnel test. The flow velocity was 33 m/sec and the average dynamic viscosity was 0.151 cm<sup>2</sup>/sec. Velocity measurements were taken at twenty-three locations ranging from 0.087 m to 4.987 m from the leading edge. The boundary thickness grew from 0.0335 cm to 0.9242 cm. The test data were compiled and presented at a 1968 Stanford turbulent flow conference<sup>15</sup>.

In the present computation, the computational domain extends 8 m in streamwise direction, 0.16 m in cross flow direction, and 0.5 m in the third direction; grid points used are 57, 61 and 5 in the respective directions. The Reynolds number (Re) is  $2.2 \times 10^6$ . Grid distribution in the cross-flow direction is non-uniform, and is clustered near the plate such that the  $y^+$  coordinate of the first grid point off the plate surface is less than 0.3. The Courant-Friedrichs-Lewy (CFL) number for present computations is  $10^3$ . For the turbulence modelling, the standard Baldwin and Lomax's algebraic eddy viscosity formulation<sup>16</sup> is used. Figure 1a shows the skin friction coefficient  $C_\tau$  along the plate surface, and Figs. 1b and 1c show the axial velocity profiles at  $x=0.78$  m and 4.98 m, respectively. The RMS differences indicate that the deviations between the measurements and the predictions are within the limits of the expected measurement

uncertainties. Figure 2 shows the velocity profile at  $x=4.98$  m presented in  $(y^+, u^+)$  coordinates. It can be seen that the predictions agree well with the measurements. In the turbulent zone where  $y^+$  lies between 30 and 1000, both the predictions and the measurements fit the universal logarithmic law. However, none of the data lie within the sublayer. The convergence history presented in Fig. 3 shows that the residual value approaches the machine zero.

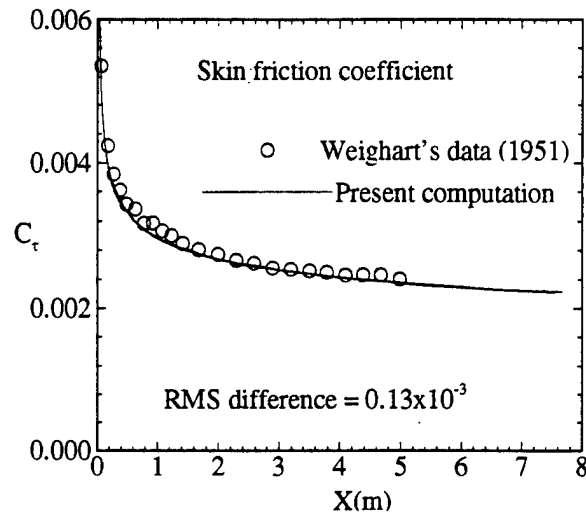


Fig. 1a. Skin friction coefficient.

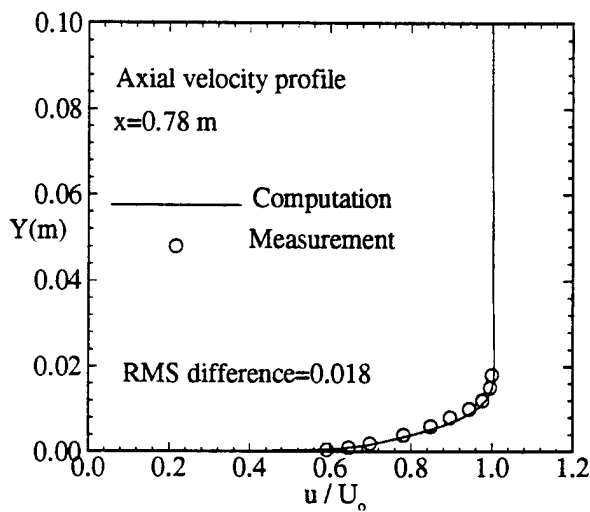


Fig. 1b. Velocity profile at  $x=0.78$  m.

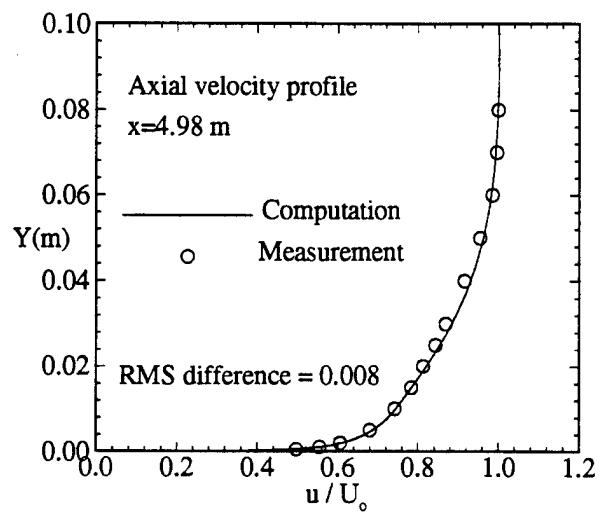


Fig. 1c. Velocity profile at  $x=4.98$  m.

Fig. 1. Skin friction coefficient and velocity profile for turbulent flow along a flat plate.

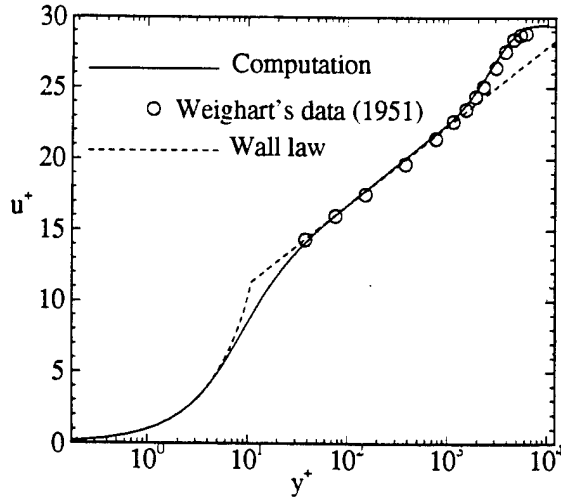


Fig. 2. Velocity profile in  $(y^+, u^+)$  coordinates.

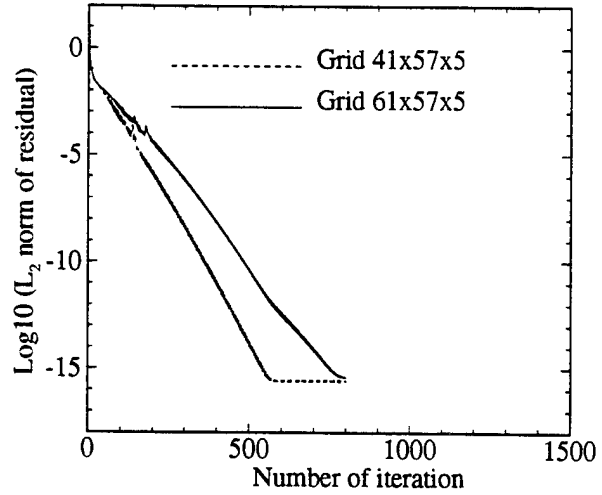


Fig. 3. Convergence histories for computing turbulent flow along a flat plate.

### LAMINAR FLOW ALONG A FLAT PLATE

For steady laminar flow along a flat plate with a constant free stream velocity  $U_o$ , the pressure gradient  $\partial p/\partial x$  in streamwise direction vanishes. The Navier-Stokes equations reduce to the Prandtl boundary-layer equations. A solution, known as the Blasius solution after its originator, is obtained by assuming similar profiles along the plate at every location along the plate. Blasius assumed that

$$\frac{u}{U_o} = F\left(\frac{y}{\delta}\right),$$

where  $y$  is the distance above the plate surface,  $\delta$  is the boundary layer thickness, and

$$\frac{y}{\delta} \sim \frac{y}{x/\sqrt{R_x}} = \eta,$$

with  $x$  the distance from leading edge and  $R_x$  the Reynolds number based on  $x$ . Under the similarity assumption, the Prandtl boundary layer equations can be further reduced to an ordinary differential equation. Solution can then be obtained numerically. In the present numerical simulation, the geometrical dimension used previously for turbulent flow is adopted and the Reynolds number is  $3.64 \times 10^5$ . The grid size is  $129 \times 129 \times 3$ . Figure 4a shows the skin friction coefficient along the plate surface, and Figs. 4b and 4c show the profiles of axial velocity  $u/U_o$ , and transverse velocity  $w/U_o$ , respectively. The RMS difference for each quantity is also presented. The results of the present

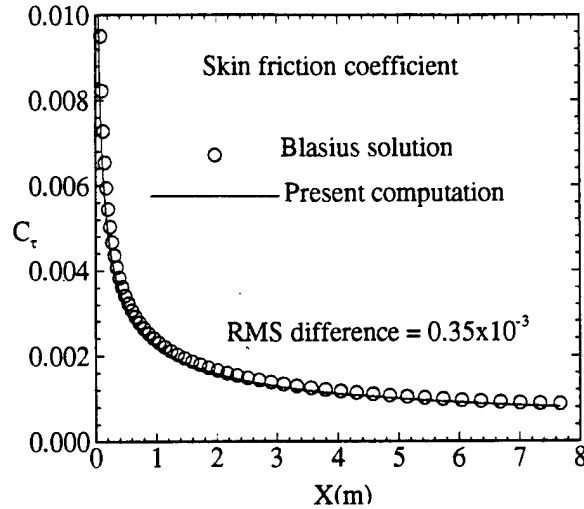


Fig. 4a. Skin friction coefficient.

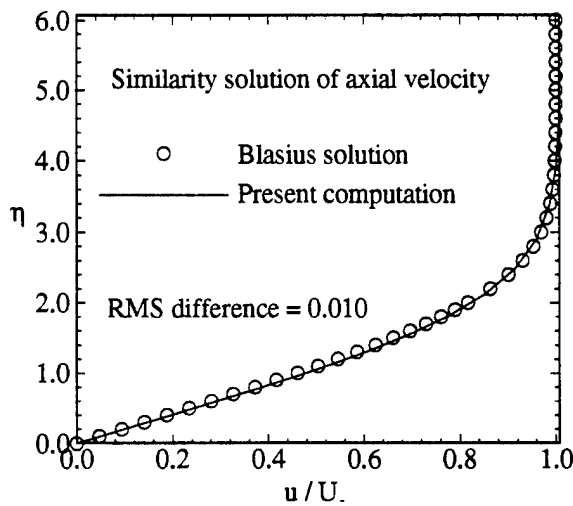


Fig. 4b. Axial velocity profile.

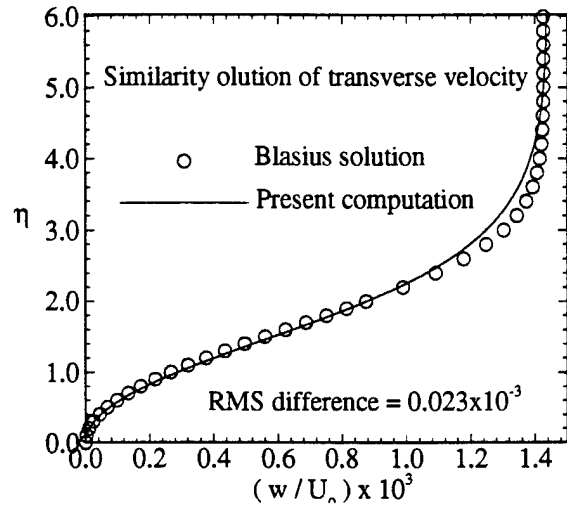


Fig. 4c. Transverse velocity profile.

Fig. 4. Skin friction coefficient and velocity profiles for laminar flow along a flat plate.

computation agree well with the solutions obtained by Blasius's method. Part of the deviation can be attributed to the fact that the Blasius's solution is based on Prandtl boundary layer equations while the current computation is based on Navier-Stokes equations. Figure 5 shows the convergence histories for solutions with multigrid (7 levels) and without multigrid (1 level) application. Considerable computing effort is saved with the application of the multigrid method.

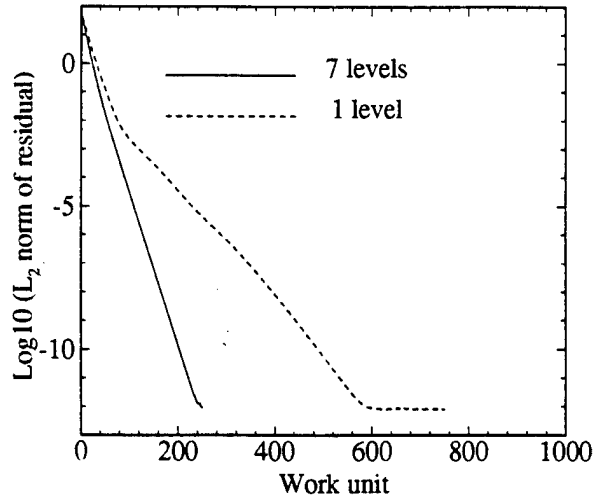


Fig. 5. Convergence histories for computing laminar flow along a flat plate.

## FLOW PAST CIRCULAR CYLINDERS AT LOW SPEEDS

For flow past a circular cylinder at Reynolds numbers (length scale is based on the diameter) below the critical value ( $\sim 40$ ) at which a Kármán street is formed, the flow is steady and twin vortices exist behind the cylinder. There are many interesting flow related phenomena despite the simplicity of the geometry involved. The phenomena are the boundary layer development along curved surface, the flow separation, and wake reattachment. However, the details of these phenomena, such as the locations of the separation, the coordinates of the vortex center, and the wake's length and shape, are Reynolds numbers dependent and pose great challenges for numerical simulation. For these and other reasons, this problem has drawn much attention in the past, both theoretically and experimentally. In light of the availability and quality of the data, this problem is selected as a benchmark case for present numerical study.

The outer boundary of the computational domain is described by a circle with a radius 10 times that of the cylinder. An O-type and orthogonal grid system is selected. The grid distribution in the radial direction is non-uniform and is clustered near the surface. The distance between the cylinder surface and the first grid point is one-thousandth of the radius of the cylinder. For computation, symmetry is assumed and only the plane above the axis of symmetry is considered. The number of grid points in radial, circumferential and axial directions are 257, 257 and 3, respectively. The CFL number used for the following computations is  $10^2$ . The boundary conditions are: (1) a non-slip, non-penetrating, and vanishing normal pressure gradient on solid surface, (2) prescribed free stream values at the upstream side of the outer boundary, (3) second-order extrapolations at the downstream side of the outer boundary and (4) periodicity in the spanwise direction. In order to describe the main features of the flow,

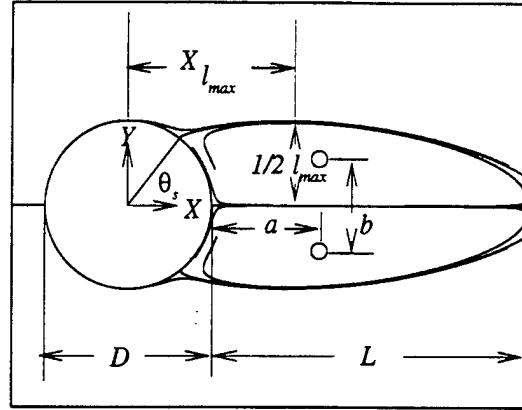


Fig. 6. Geometrical parameters of the closed wake.

Coutanceau and Bouard's<sup>17</sup> geometrical parameters for the closed wake are adopted and shown in Fig. 6, where parameters  $l$  and  $L$  are the width and length of the wake,  $\theta_s$  is the separation angle and the vortex centers are located on the  $(x, y)$  axes by  $a$  and  $b$ . It was observed by Taneda<sup>18</sup> that the twin vortices behind the cylinder appeared when the Reynolds number was greater than 6 and became unstable when the Reynolds number was greater than 45. Therefore, the Reynolds numbers 5 and 40 are selected as the lower and upper bounds for the present steady-state computations. Taneda's<sup>18</sup> and Coutanceau and Bouard's<sup>17</sup> flow visualizations were obtained by similar methods: by illuminating the light particles suspended uniformly in the liquid and by photographing in the direction normal to the lighted plane. Taneda<sup>18</sup> used aluminium and water in the tests, while Coutanceau and Bouard<sup>17</sup> used fine bright particles and the Vaseline oil ' MARCOL 80 ' in their tests. The latter reference derived the particle velocity by measuring the length of the particle trajectory during the time of exposure. The reported inaccuracy was less than 2%. The wall influence was investigated by changing the ratio  $\lambda$  between the cylinder and the tank diameters<sup>17</sup>. Figure 7 shows the computed wake shapes behind the cylinder at different Reynolds numbers. Compared with the flow visualizations<sup>17, 18</sup>, the characteristics of the wake shapes near the separation and reattachment points are well simulated. The result indicates that the twin vortices begin to develop at Reynolds number about 5 and it agrees with Taneda's<sup>18</sup> observation. In Fig. 8, the currently computed separation angles at various Reynolds numbers are compared with those computed earlier by Keller<sup>19, 20</sup> and Raal<sup>21</sup> and those measured by Coutanceau and Bouard.<sup>17</sup> Figure 9 shows the relationship between the Reynolds numbers  $Re$  and the wake lengths  $L/D$ , from both the current computations

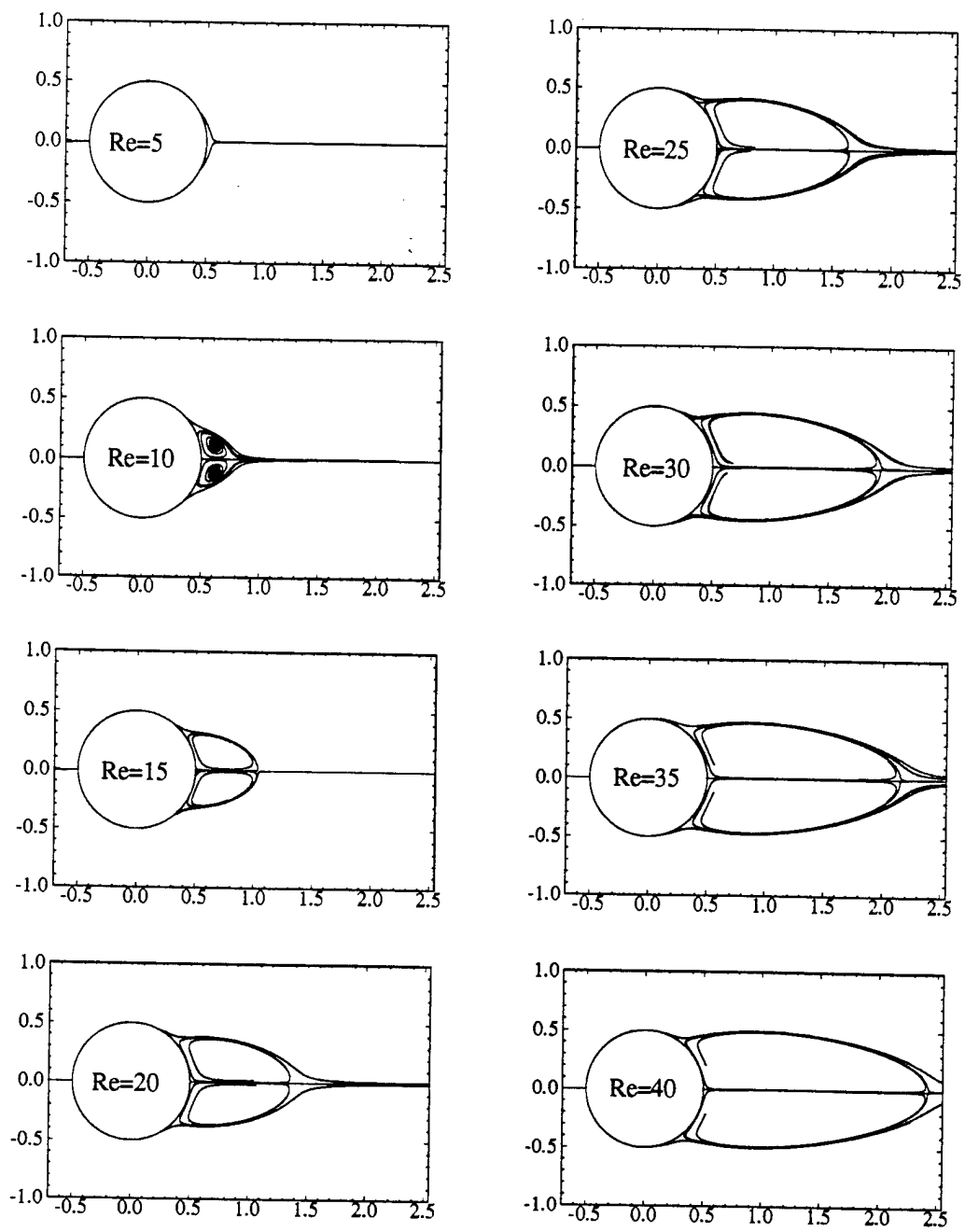


Fig. 7. Standing vortices downstream of a circular cylinder.

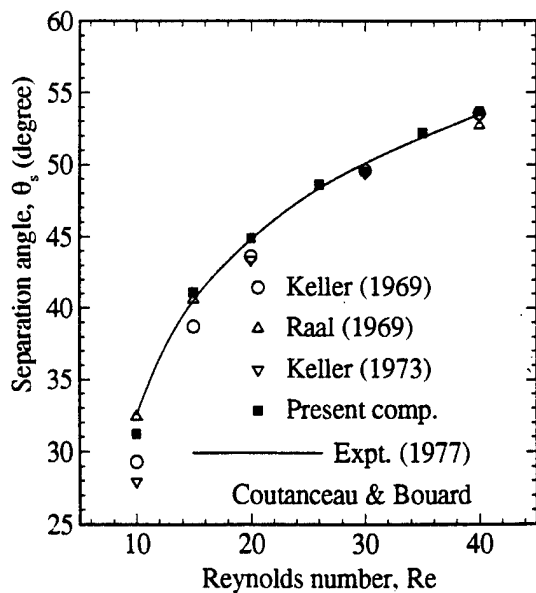


Fig. 8. Separation angles at different Reynolds numbers for flow past a circular cylinder.

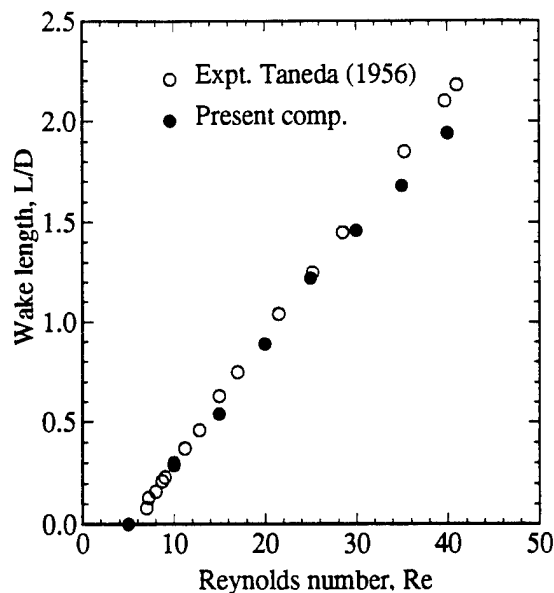


Fig. 9. Wake lengths at different Reynolds numbers for flow past a circular cylinder.

and Taneda's observations.<sup>18</sup> In Fig. 10, the coordinates of the vortex center ( $a, b$ ) (see Fig. 6) are plotted against the Reynolds number,  $Re$ . The experimental data were reported by Coutanceau and Bouard<sup>17</sup> with  $\lambda$ , the ratio between the cylinder and the tank diameters, equal to 0.024. The small value of  $\lambda$  indicates that the wall effect is relatively small. Figure 11 shows the similarity of the closed-wake shape.<sup>17</sup> For computed and measured wakes at different Reynolds numbers, when the wake width  $l$  and its distance from the rear stagnation point  $X - R$ , are normalized with the maximum wake width  $l_{max}$  and wake length  $L$ , respectively, and then plotted against each other, the results merge into a single curve except at the regions near the cylinder wall. Figure 12 shows the velocity similarity on the rear flow axis in the closed wake, where the velocity  $u$  is normalized with its maximum value  $u_{max}$ . Figure 13 shows the comparisons of the computed and measured velocities at rear flow axis at Reynolds numbers 20 and 40. The RMS differences are comparable with the measurement uncertainty ( $\sim 2\%$ ). Figure 14 shows the computed pressure distribution at the cylinder surface for  $Re=40$ ; it is compared with the distributions observed at  $Re=36$  and  $Re=45$  by Thom,<sup>22</sup> and computed by Apelt<sup>23</sup> at  $Re=40$ . Thom's approximate theory<sup>24</sup> for determining the value of the pressure at the front stagnation point at low speed gives the result at Reynolds number 40,  $(1+7/Re)$  or 1.175, which agrees well with the value of the current result 1.18. Figure 15 presents the convergence histories of the numerical simulation at  $Re=40$ . The 7-level multigrid solver improves the efficiency significantly. A fine grid size is needed for detailed computation, because with such a fine grid size the convergence is slow. The application of multigrid technique (7 levels) reduces the computational effort considerably for a given CPU time.

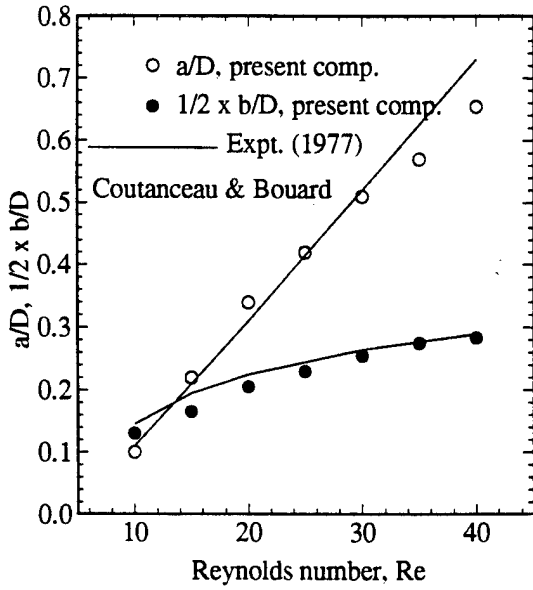


Fig. 10. Locations of vortex centers of wakes at different Reynolds numbers.

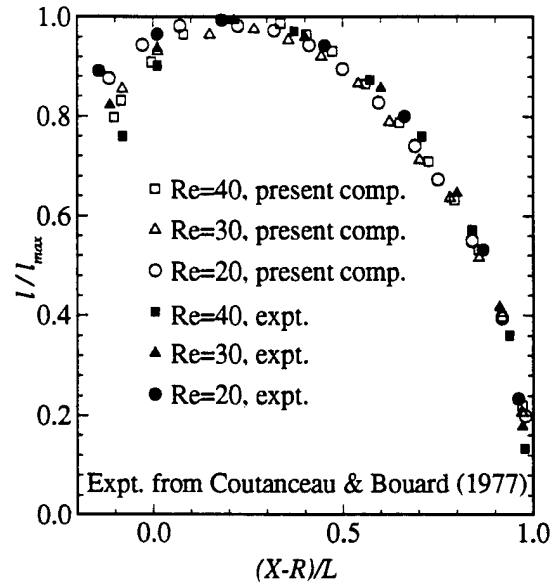


Fig. 11. Similarity of the closed-wake shapes.

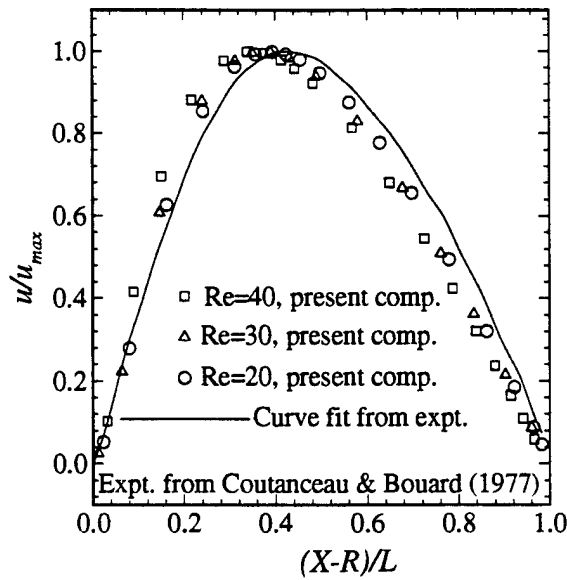


Fig. 12. Velocity similarity on the rear flow axes of the closed wakes.

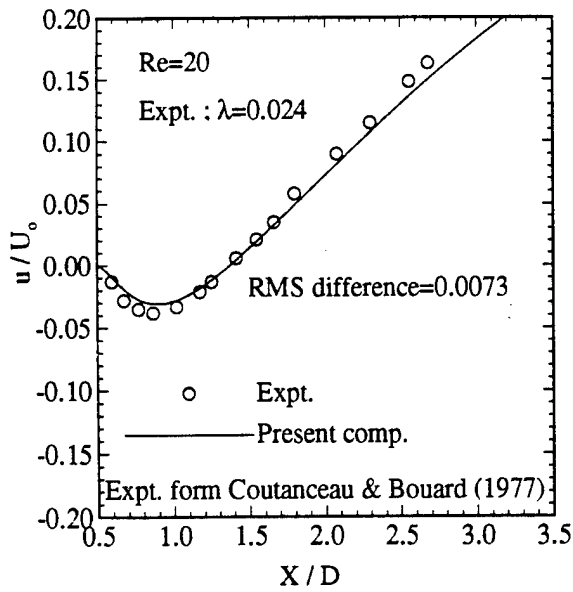


Fig. 13a. Re=20.

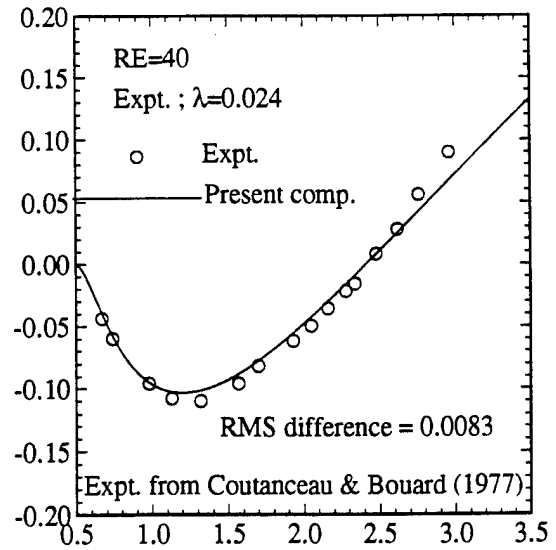


Fig. 13b. Re=40.

Fig. 13. Velocity distributions on the flow axis behind the circular cylinder.

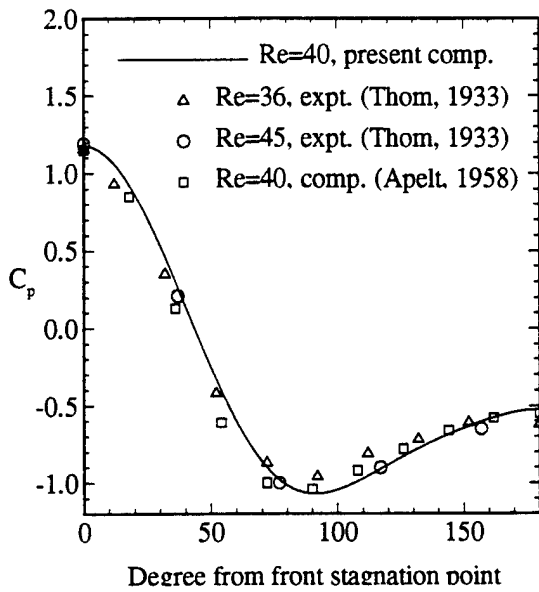


Fig. 14. Surface pressure distribution for flow past a circular cylinder at Re=40.

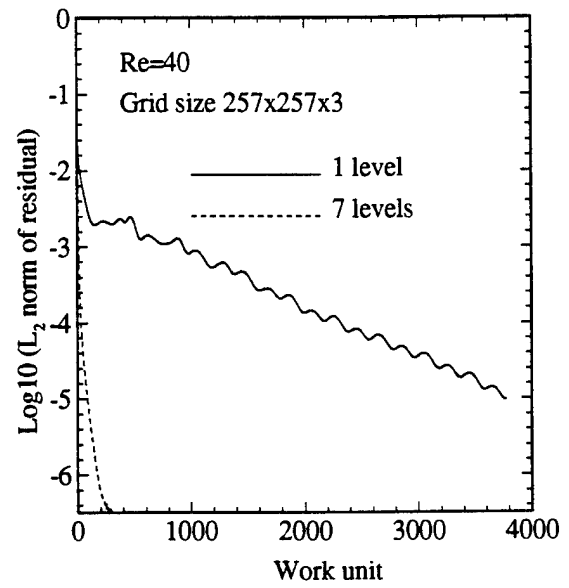


Fig. 15. Convergence histories for computing flow past a circular cylinder at Re=40.

## FLOW PAST SPHERES AT LOW SPEEDS

The flow and the solutions are assumed to be axisymmetric. The topology of the grid and the specification of the boundary conditions are the same as those used for computing the flow over the cylinder presented earlier, except that the reflective condition is applied in the circumferential direction. The solutions on different meridional planes are related by simple coordinate transformation. The CFL number used for the computations is  $10^2$ . Figure 16 shows the computed wake shapes behind the sphere at various Reynolds numbers. The relationship between the Reynolds number  $Re$  and the

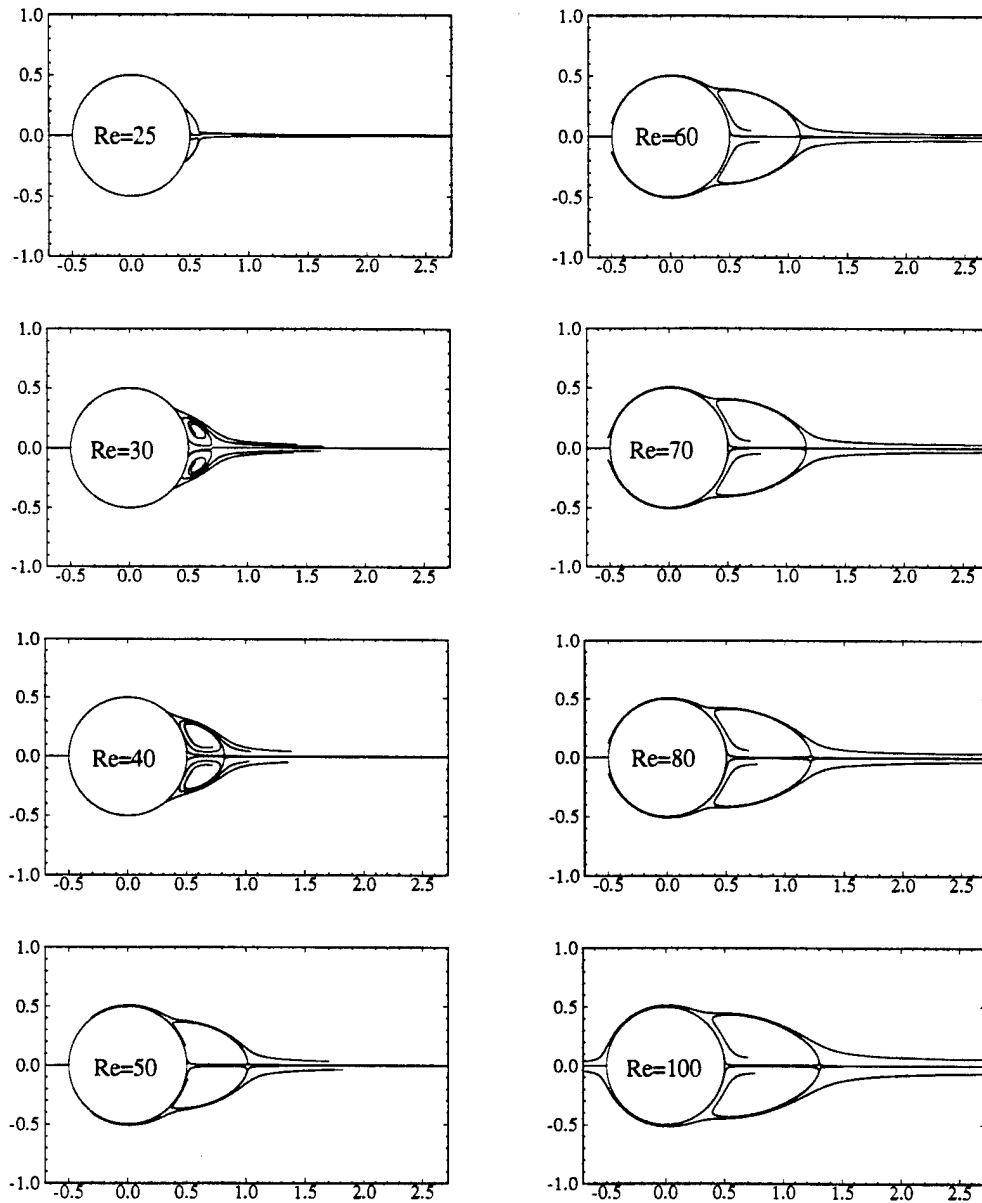


Fig. 16. Standing vortices downstream of a sphere.

wake length  $L$  is plotted in Fig. 17; also included are the test data from Taneda.<sup>25</sup> The twin vortices behind the sphere appear at Reynolds number about 25. The surface pressure distribution at Reynolds number 100 is shown in Fig. 18; also included are the results from earlier computations.<sup>26, 27</sup> The convergence histories for  $Re=100$  is shown in Fig. 19. Multigrid technique improves the computational efficiency significantly.

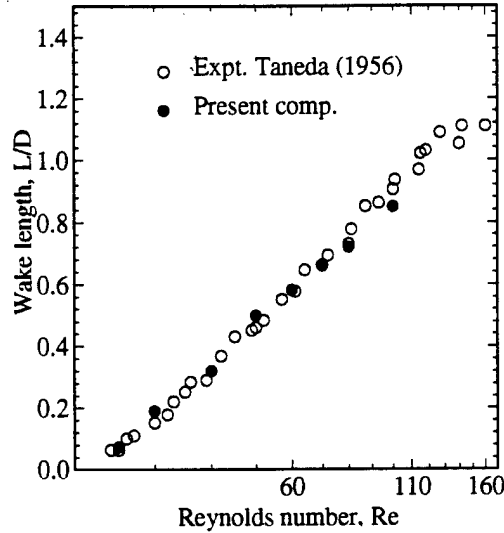


Fig. 17. Wake lengths at different Reynolds numbers for flow past a sphere.

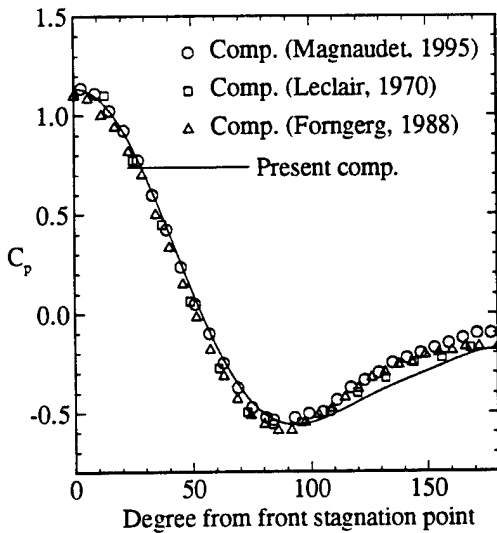


Fig. 18. Surface pressure distribution for flow past a sphere at  $Re=100$ .

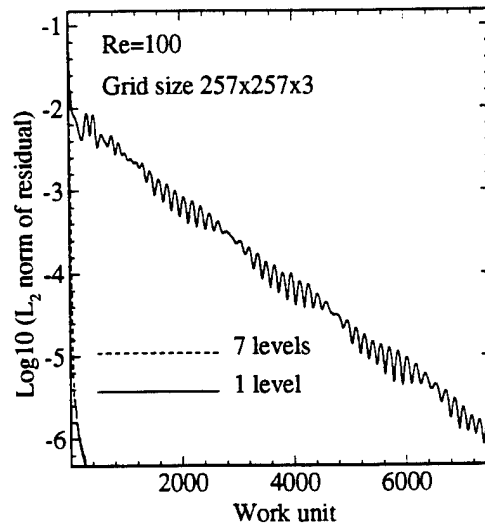


Fig. 19. Convergence histories for computing flow past a sphere at  $Re=100$ .

## TURBULENT FLOW PAST AXISYMMETRIC BODIES

The purpose of this computation is to investigate the accuracy of the numerical scheme in predicting the characteristics of the flow in an expanding boundary layer under adverse pressure gradient at high Reynolds numbers. Axisymmetric bodies, designated as DTMB-body1 and DTMB-body2, were built and tested at the David Taylor Model Basin (DTMB)<sup>28</sup>. The Reynolds number at the test condition was  $6.6 \times 10^6$ . The size of the C-type grid for the present computation is  $197 \times 3 \times 146$  in radial, circumferential and axial directions, respectively. Modified Baldwin-Lomax model<sup>2</sup> is used to simulate the turbulent flow. Figure 20 shows the computed (solid line) and measured (symbol) pressure distributions on surface of DTMB-body1. The RMS difference is 0.019. The measurement uncertainty for pressure was  $\pm 0.015$ . It can be seen that the pressure gradient is zero at the parallel mid-body region, and adverse gradient is present at stern region. In Fig. 21 the computed velocity profiles at various axial locations at stern region of DTMB-body1 are compared with the measurements. The RMS differences range from 0.012 to 0.025. The measurement uncertainty for velocity was  $\pm 0.025$ . In Fig. 22 the velocity profiles, at the parallel mid-body section, are plotted in the  $(y^+, u^+)$  coordinates. The value of the  $y^+$  of the grid nearest to the body surface is about 2.5. There are four grid points that lie within the laminar sublayer. The computed distribution of skin friction (solid line) on body surface is shown in Fig. 23. Compared with the measurements, the RMS difference is 0.00029. The measurement uncertainty for skin friction was  $\pm 0.0002$ . The computed (solid line) and measured (symbol) turbulence shear stresses near the stern region at several axial locations are shown in Fig. 24; the RMS differences range from 0.008 to 0.015. The measurement uncertainty for turbulent shear stresses is  $\pm 0.01$ .

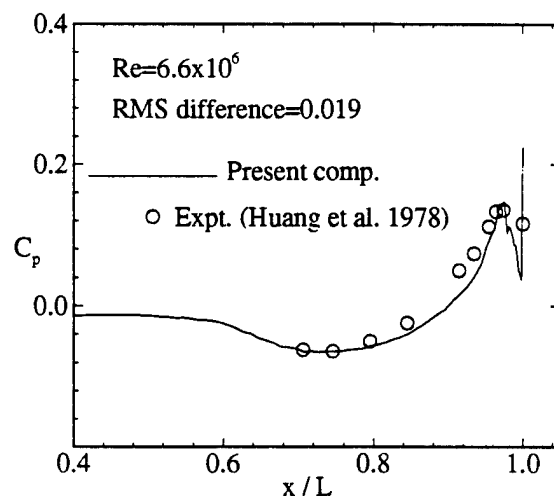


Fig. 20. Surface pressure distribution for DTMB-body1.

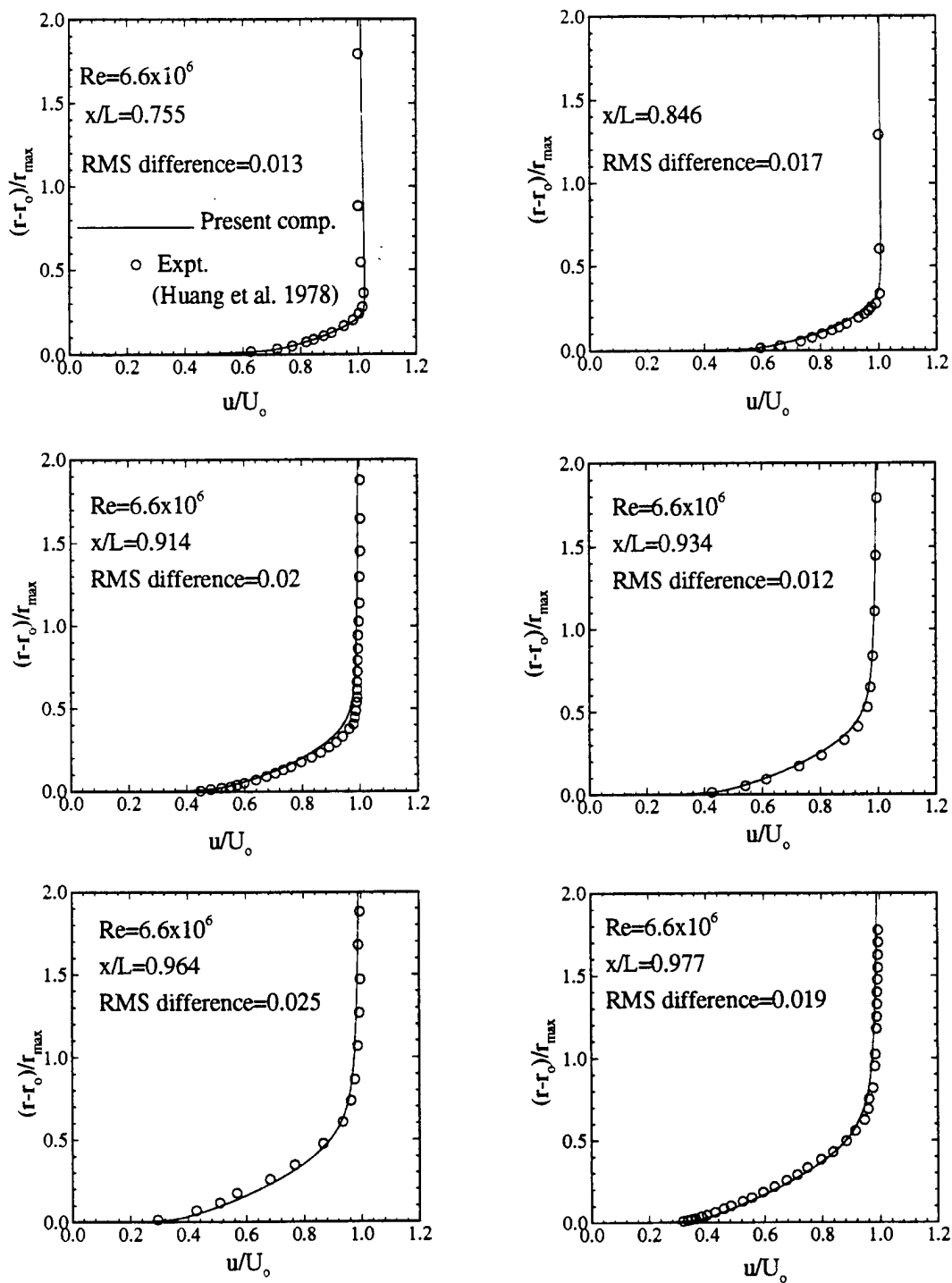


Fig.21. Velocity profiles at stern region of DTMB-body1.

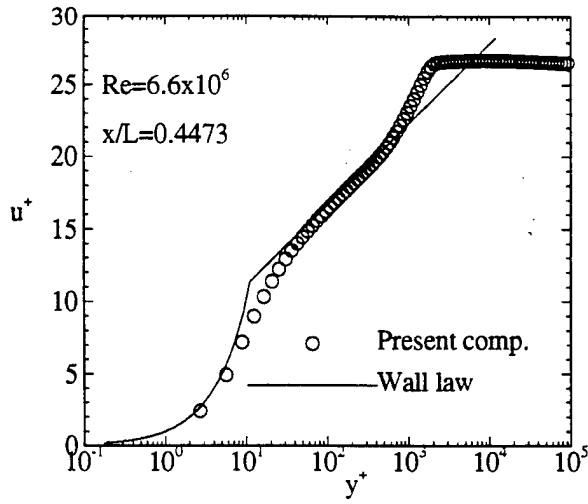


Fig. 22a.  $x/L=0.4473$

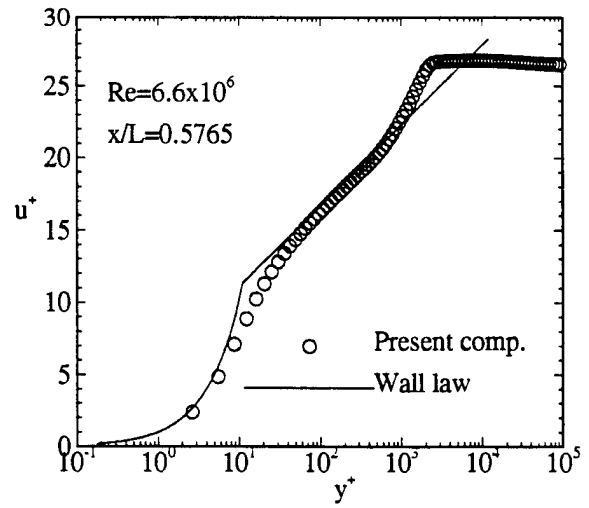


Fig. 22b.  $x/L=0.5765$

Fig. 22. Comparisons of wall law at mid-body section of DTMB-body1.

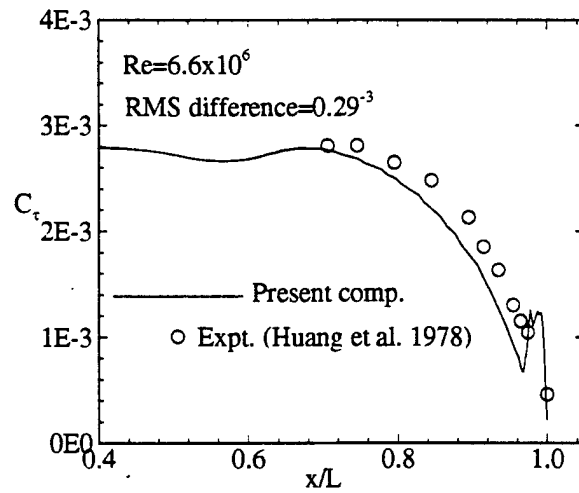


Fig. 23. Skin friction coefficient along the surface of DTMB-body1.

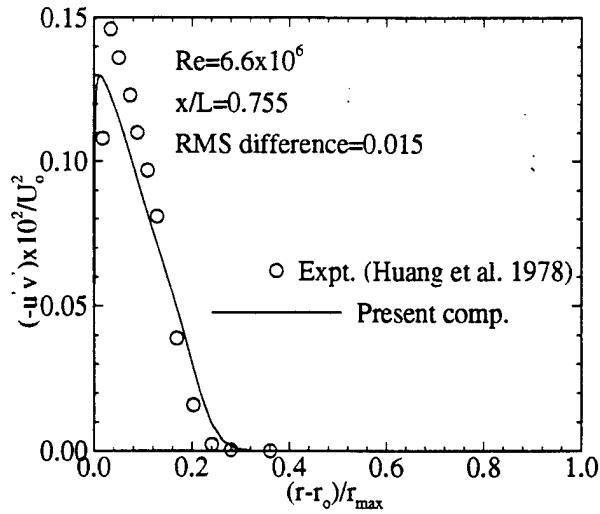


Fig. 24a.  $x/L=0.755$ .

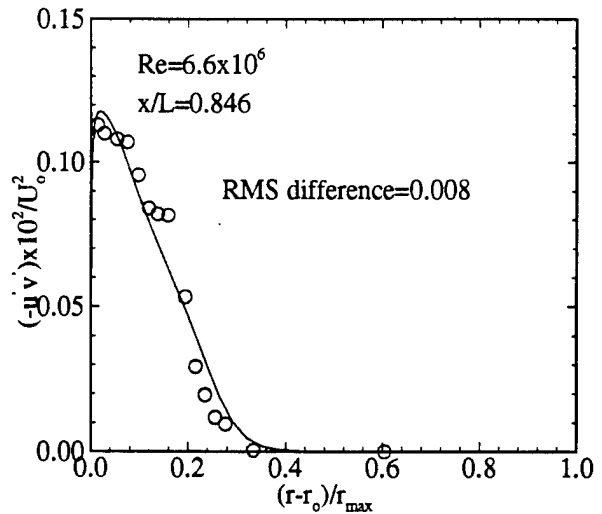


Fig. 24b.  $x/L=0.846$ .

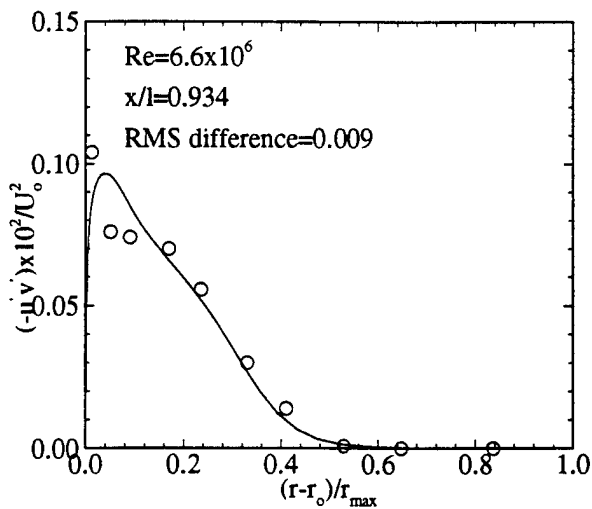


Fig. 24c.  $x/L=0.934$ .

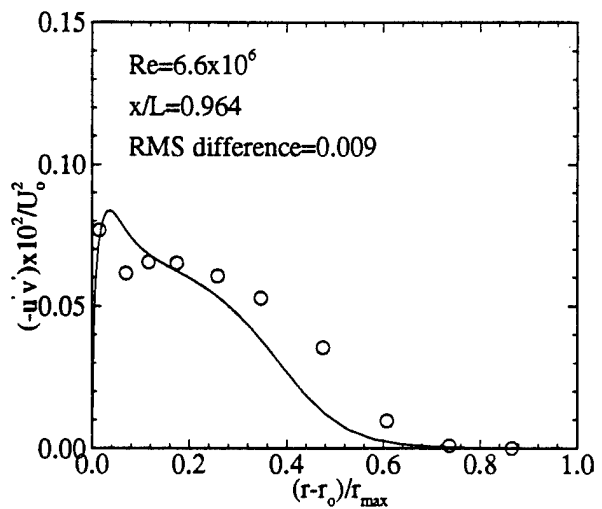


Fig. 24d.  $x/L=0.964$ .

Fig. 24. Turbulent shear stresses near the stern region of DTMB-body1.

A propeller was placed on DTMB-body1 whose center line is located at  $x/L=0.983$ . The ratio of propeller and body diameter is 0.54. Velocity measurements were taken at a distance of 0.227 propeller diameter upstream of the propeller. For numerical prediction, the propeller effect was simulated with a body force model. The computed and measured velocity profiles under two different propeller operating conditions are shown in Fig. 25.

The same type of computations were carried out on DTMB-body2. The velocity profiles at different axial locations are shown in Fig. 26. The RMS differences between the computed and measured values range from 0.008 to 0.058.

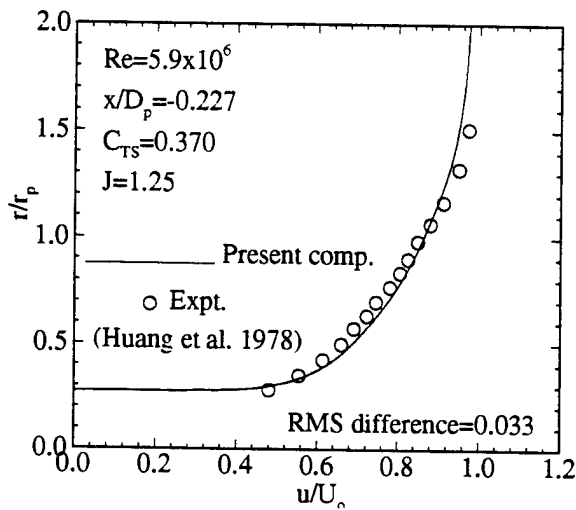


Fig. 25a. Advance ratio=1.25.

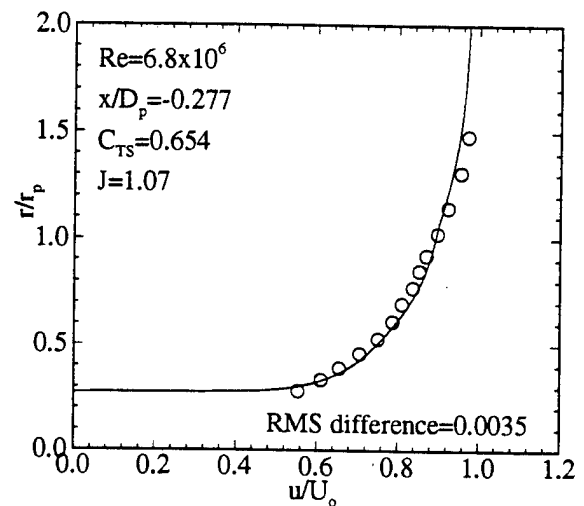


Fig. 25b. Advance ratio=1.07.

Fig. 25. Velocity profiles upstream of an operating propeller at different advance ratios.

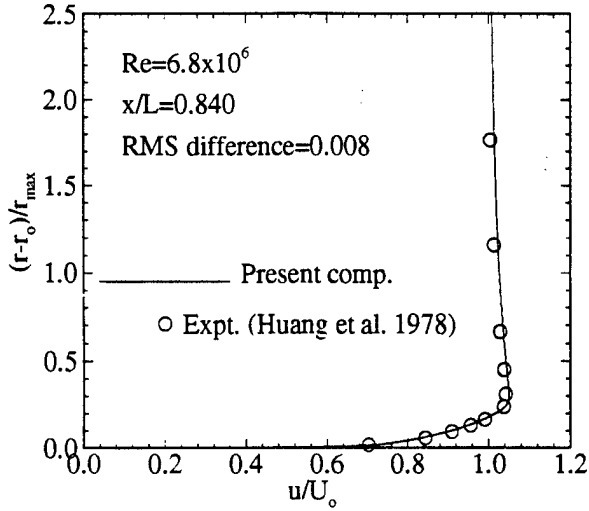


Fig. 26a.  $x/L=0.840$ .

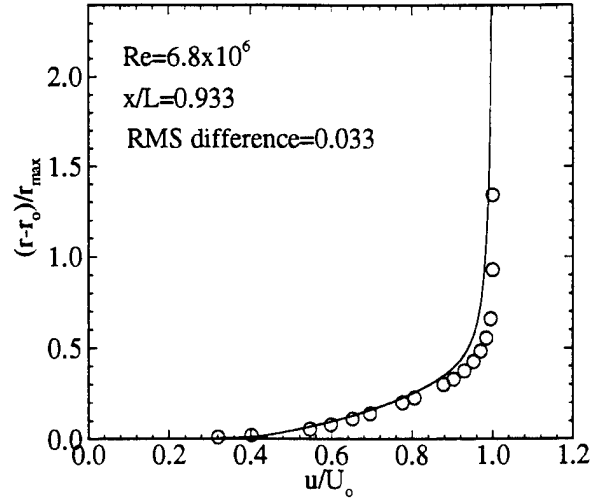


Fig. 26b.  $x/L=0.933$ .

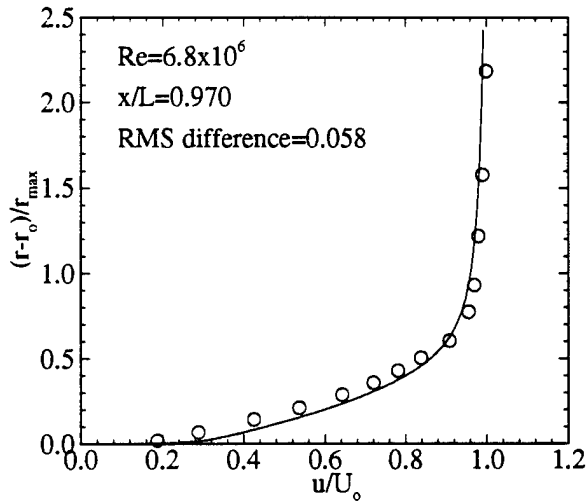


Fig. 26c.  $x/L=0.970$ .

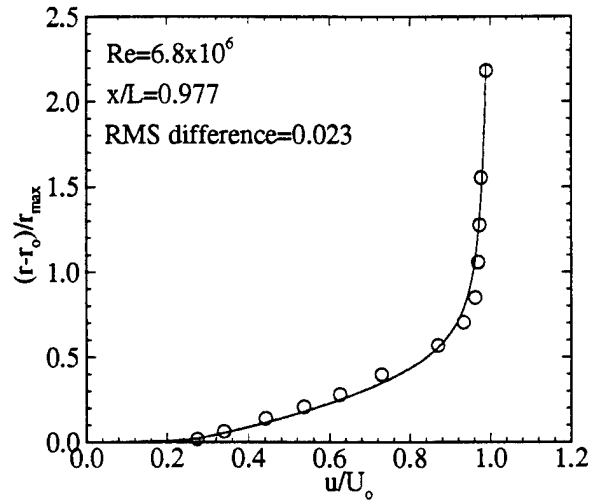


Fig. 26d.  $x/L=0.977$ .

Fig. 26. Velocity profiles at stern region of DTMB-body2.

## CONCLUSIONS AND RECOMMENDATIONS

An upwind, high-resolution, finite-differencing Navier-Stokes solver is used to simulate steady-state incompressible flows with a wide range of Reynolds numbers. Experiments with measurements of high quality are selected as benchmark cases. The predictions are compared with the measurements by evaluating the root mean square (RMS) differences. In all cases, the RMS differences are compatible with the measurement uncertainties. For the low Reynolds number cases, the detailed features of the standing vortices behind the bluff bodies are successfully simulated. For the high Reynolds number cases, the skin friction coefficients, the structure of the turbulent velocity profiles and the turbulent shear stresses are correctly predicted.

At low Reynolds numbers, the flows are dominated by diffusive process. The rate of convergence of the iterative procedure becomes very slow, even for an implicit method with a rather high CFL number. The situations can be improved significantly by implementing the multigrid technique. Compared with the single-grid approach, the multigrid solver is rather insensitive to the CFL numbers and an order of magnitude of Central Processor Unit (CPU) time is saved.

In summary, the flow features that are relevant to the propulsor analysis, such as flow separation and reattachment, surface pressure and skin friction distributions, can be predicted accurately and efficiently with an upwind RANS solver. The formulations of DTNS<sup>1</sup> are similar to the formulations described in this report. It is expected that DTNS<sup>1</sup> code may achieve the similar performances. For complicated turbulent flows, to correctly predict the turbulent structures, a sophisticated non-equilibrium turbulence model is needed.

## REFERENCES

1. Gorski, J.J., "TVD Solution of the Incompressible Navier-Stokes Equations with an Implicit Multigrid Scheme," *AIAA* paper 88-3699 (1988).
2. Sung, C.H., "Recent Progress in Incompressible Reynolds Averaged Navier-Stokes Solver," Presented at the International Conference on Hydrodynamics, Wuxi, China (1994).
3. Hartwich, P-M, and Hsu, C-H, "High-Resolution Upwind Scheme for the Three-Dimensional Incompressible Navier-Stokes Equations," *AIAA Journal*, Vol. 26, No. 11 (Nov 1988).
4. Yang, C-I., "A simulation of viscous Incompressible Flow Through a multiple-Blade-Row turbomachinery with a High-Resolution Upwind Finite Differencing scheme," *Numerical Simulations in Turbomachinery* ASME FED-Vol. 227, pp.11-18 (1995)

5. van Leer, B., "Towards the Ultimate Conservative Difference Scheme, III. Upstream-Centered Finite Difference Schemes for Ideal Compressible Flow," *Journal of Computational Physics*, Vol. 23, pp.263-275 (1977).
6. Roe, P. L., "Approximate Riemann Solvers, Parameter Vectors, and Difference Scheme," *Journal of Computational Physics*, Vol. 43, No. 2, pp. 357-372 (1981).
7. Yee, H., "On the Implementation of a Class of Upwind Schemes for System of Hyperbolic Conservation Laws," *NASA Technical Memorandum 86839* (1985).
8. Chorin, A., "A Numerical Method for Solving Incompressible Viscous Flow Problem," *Journal of Computational Physics*, Vol. 2, pp. 2-26 (1967).
9. Pulliam, T.H., Steger, J.L., "On Implicit Finite-Difference Solutions of Three-Dimensional Flow," *AIAA paper 78-10*, (1978).
10. Yee, H., Warming, R.F., Harten, A., "Implicit Total Variation Diminishing (TVD) Schemes for Steady-State Calculations," *Journal of Computational Physics*, Vol. 57, pp. 327-360 (Sept 1985).
11. Roe, P.L., "Some Contributions to the Modelling of Discontinuous Flow," *Lecture in Applied Mathematics*, Vol. 22, pp. 163-193 (1985).
12. Brandt, A., "Multigrid Techniques: 1984 Guide with Application to Fluid Dynamics," *Lecture Note for the CFD Lecture Series at VKI*, (1984).
13. Ludwig, H., Tillmann, W., "Investigation of the Wall Shearing Stress in Turbulent Boundary Layers," *NACA TM 1285*, (1951).
14. Wieghart, K., Tillmann, W., "On the Turbulent Friction Layer for Rising Pressure," *NACA TM 1314* (1951).
15. Coles, D.E., Hirst, E.A., "Proceedings, Computation of Turbulent Boundary Layer-1968 AFOSR-IFP-Stanford Conference," *Volume II, Compiled Data*, (1968).
16. Baldwin, B.S., Lomax, H., "Thin Layer Approximation and Algebraic Model for Separated Turbulent Flow," *AIAA Paper No. 78-257* (1978).
17. Coutanceau, M., Bouard, R., "Experimental Determination of the Main Features of the Viscous Flow in the Wake of a Cylinder in Uniform Translation. Part 1. Steady Flow," *J. Fluid Mech.*, Vol. 79, Part 2, pp. 231-256 (1977).
18. Taneda, S., "Experimental Investigation of Wake behind Cylinders and Plates at Low Reynolds Number," *Journal of the Physical Society of Japan*, Vol.11, No.3 pp. 302-307 (1956).

19. Takami, H., Keller, H.B., "Steady Two-Dimensional Viscous Flow of an Incompressible Fluid Past a Circular Cylinder," *Phys. Fluids Suppl.*, Vol. 12, II 51 (1969).
20. Nieuwstadt, F., Keller, H.B., "Viscous Flow Past Circular Cylinders," *Computers and Fluids*, Vol.1, 11 (1973)
21. Hamielec, A.E., Raal, J.D., "Numerical Studies of Viscous Flow Around Circular Cylinders," *Phys. Fluids*, Vol. 12, 11 (1969).
22. Thom, A., "The Flow Past Circular Cylinders at Low Speeds," *Proc. Roy. Soc. , A*, Vol. 131, pp. 651-669 (1933).
23. Apelt, C.J., *Aero. Res. Counc. R and M No.3175* (1958).
24. Thom, A., "The Pressure on the Front Generator of a Cylinder," *Aero. Res. Counc. R and M No.1389* (1930).
25. Taneda, S., "Experimental Investigation of the Wake behind a Sphere at Low Reynolds Numbers," *Journal of the Physical Society of Japan*, Vol.11, No.10, pp. 1101-1108 (1956).
26. Magnaudet, J., Rivero, M., Fabre, J., "Accelerated Flows Past a Rigid Sphere or a Spherical Bubble. Part 1. Steady Straining Flow," *J. Fluid Mech.*, Vol. 284, pp. 97-135 (1995).
27. Fornberg, B., "Steady Viscous Flow Past a Sphere at High Reynolds number," *J. Fluid Mech.*, Vol. 190, pp. 471-489 (1988).
28. Huang, T.T., Santelli, N., Belt, G., "Stern Boundary-Layer Flow on Axisymmetric Bodies," *12th symposium on Naval Hydrodynamics Washington D.C.*, pp. 127-157 (1978).



## INITIAL DISTRIBUTION

Copies	Code	Name	Copies	Code	Name
1	ARPA	G. Jones	4	PSU/ARL	
6	ONR		1	C. Knight	
	1	333 J. Fein	1	McBride	
	1	333 P. Majumdar	1	D. Thompson	
	1	333 P. Purtell	1	W. Zierke	
	1	333 E. Rood			
	1	334 A. Tucker			
	1	334 R. Vogelsong			
1	OPNAV				
	1	N87S J. Schuster	1	0114	K. Kim
8	NAVSEA		1	50	W.B. Morgan
	1	03H E. Comstock	1	508	R. Boswell
	2	03X R. Crockett	1	508	J. Brown
	1	03T M. Nicholson	1	508	R. Cross
	1	PEO-SUB R A. Spero	1	508	H. Liu
	1	PEO-SUB R M. Troffer	1	521	W. Day
	1	PEO-SUB R E. Robinson	1	542	J. Gorski
	1	PEO-SUB X L. Becker	1	542	C-H Sung
	1	PEO-SUB X D. Goldstein	1	542	H. Haussling
			1	542	Y.-T. Lee
2	NUWS		1	544	F. Peterson
	1	P. Lefebvre	1	544	C. Dai
	1	J. Uhlman	1	544	B. Chen
2	DTIC		1	544	S. Neely
			1	544	D. Fuhs
			1	544	C-I Yang
1	Science Applications		1	7051	W. Blake
International Corp.			1	7200	Y-F Hwang
	1	R. Korpus			
3	MIT/Dept. Ocean Eng.		1	3421	TIC (C)
	1	D. Keenan			
	1	J. Kerwin			
	1	S. Kinnas			
1	Newport News Shipbuilding				
	1	J. DeNuto			
1	General Dynamics/EB Div.				
	1	M. King			
1	Arete Associates				
	1	T. Brockett			

### CENTER DISTRIBUTION